



**Visualising Discrete Structural Transformations in Germanium Nanowires during Ion Beam Irradiation and Subsequent Annealing**

Journal:	<i>Nanoscale</i>
Manuscript ID:	NR-ART-08-2014-004513.R1
Article Type:	Paper
Date Submitted by the Author:	21-Aug-2014
Complete List of Authors:	Kelly, Roisin; Tyndall National Institute, University College Cork, Chemistry Holmes, Justin D.; Tyndall National Institute, University College Cork, ; Centre for Research on Adaptive Nanostructures and Nanodevices (CRANN), Trinity College Dublin, Petkov, Nikolay; Tyndall National Institute, University College Cork,

## ARTICLE

# Visualising Discrete Structural Transformations in Germanium Nanowires during Ion Beam Irradiation and Subsequent Annealing

youCite this: DOI:  
10.1039/x0xx00000x

Received 00th January 2014,  
Accepted 00th January 2014

DOI: 10.1039/x0xx00000x

[www.rsc.org/](http://www.rsc.org/)

Róisín A. Kelly,<sup>a</sup> Justin D. Holmes<sup>a,b</sup> and Nikolay Petkov<sup>a\*</sup>

In this article we detail, the application of electron microscopy to visualise discrete structural transitions occurring in single crystalline Ge nanowires upon Ga-ion irradiation and subsequent thermal annealing. Sequences of images for nanowires of varying diameters subjected to an incremental increase of the Ga-ion dose were obtained. Intricate transformations dictated by a nanowire's geometry indicate unusual distribution of the cascade recoils in the nanowire volume, in comparison to planar substrates. Following irradiation, the same nanowires were annealed in the TEM and corresponding crystal recovery followed in-situ. Visualising the recrystallisation process, we establish that full recovery of defect-free nanowires is difficult to obtain due to defects nucleation and growth. Our findings will have large implications in designing ion beam doping of Ge nanowires for electronic devices but also for other devices that use single crystalline nanostructured Ge materials such as thin membranes, nanoparticles and nanorods.

## Introduction

The irradiation of single crystalline semiconductor substrates with energetic ion beams to introduce dopants has been developed extensively over the years, turning ion implantation into a standard doping technique in semiconductor manufacturing. Single crystalline semiconductor nanowires require uniform and controllable doping for the creation of high performance devices, such as field effect transistors (FETs),<sup>1, 2</sup> advanced sensors,<sup>3, 4</sup> photovoltaic<sup>5</sup> and light emitter<sup>6</sup> devices. Specifically, nanowire devices such as junctionless multigate FETs<sup>7</sup> require a uniform distribution and high level of active dopants ( $> 1 \times 10^{19}$  atoms cm<sup>-2</sup>) within perfectly crystalline source, gate and drain regions for reliable device performance, as

demonstrated by both ab-initio simulations and experimental devices.<sup>8</sup> With the aim to achieve enhanced control over the dopant levels and their uniform distribution, ion implantation has been applied to introduce dopants in Si and Ge nanowires.<sup>9-12</sup> In particular, Ge is a potential material for logic and optoelectronic devices due to its high hole and electron mobilities.<sup>13</sup> Nonetheless, the processing of bulk and particularly nanostructured Ge, including ion implantation and subsequent crystal recovery, is still poorly understood.<sup>14-16</sup>

The interaction of the energetic ions with single crystalline nanowires, in comparison to those in bulk substrates can be considerably altered due to (i) ions impinging at different incident

angles at a surface and (ii) abrupt termination of resultant atom recoils at nanowire surfaces.<sup>17</sup> Whilst the range of ion interactions with bulk substrates, accumulated damage and impurity distribution is theoretically simulated (SRIM computer code),<sup>18</sup> through modelling nuclear collisions involving ions and recoiling atoms, the simulation of ion interactions in nanowires has only recently been developed using an extension of the SRIM code; *iradina* (ion range and damage in nanowires).<sup>17, 19</sup>

Thermal annealing is the final step required to activate the implanted dopant atoms and recover the crystallinity of the nanowire. As with bulk substrates, recrystallisation occurs via two competing mechanisms; solid phase epitaxial regrowth (SPER) and random nucleation and growth (RNG).<sup>20-23</sup> A vast number of studies have been presented on the crystallisation of amorphous silicon,<sup>12, 24-28</sup> but far fewer for germanium.<sup>14, 29, 30</sup> It has been observed, like silicon, the germanium [111] direction is the least favourable for crystallisation and (111) stacking faults are common.<sup>31</sup> It has already been predicted by molecular dynamics simulations that the recrystallisation process in nanowires can be largely influenced by the presence of interfaces which propagate the formation of stacking fault defects.<sup>32</sup> Simulations of the defect dynamics have also shown that such defects are pinned at the nanowire surface and can be a result of overlapping growth fronts.

Herein, we present, for the first time, electron microscopy data visualising discrete structural transformations incurring in single crystalline Ge nanowires upon ion irradiation and subsequent annealing. Using a procedure based on a correlative analysis approach,<sup>33</sup> we acquired sequences of TEM images following accumulated crystal damage at varying Ga-ion fluency and energy, and relate this to initial nanowire geometry and crystal structure. Subsequent crystal recovery due to thermal annealing was monitored

in real time by in-situ TEM, revealing complex re-crystallisation patterns.

## Experimental

The nanowires used in this study were grown from Ag nanoparticle seeds via a supercritical fluid process on Si substrates.<sup>15</sup> Most of the nanowires were grown in the [111] direction, a small fraction of the nanowires were grown in the [211] direction, some of which contain longitudinal defects along the [111] direction.

The carrier chip platform used for step-wise implantation/imaging of one and the same nanowire is depicted schematically in Supporting Information (SI), Fig. S1. The instruments used were a FEI Helios 600i NanoLab Dual Beam system and a JEOL 2100 HRTEM equipped with a Gatan double tilt imaging holder. The nanowires were first imaged in the TEM where the growth direction, tilt to achieve a low index zone axis and any intrinsic defects were identified. Nanowires that required tilting no more than 10 degrees in one direction, preferably along or perpendicular to their long axis were selected. The grid was then transferred to the SEM/FIB for implantation. The nanowire was located using the SEM and then orientated (stage was rotated and moved in x- and y-directions) so that the final orientation of the nanowire was the same as when it was imaged in the TEM. The pattern for implantation was defined in the ion beam window as:  $10\ \mu\text{m} \times 10\ \mu\text{m}$  area at 30 kV (5 kV), 9.7pA, 125 ns dwell time, 1 pass and with a total time of 0.316 s to achieve a dose of  $1.9 \times 10^{13}$  ions  $\text{cm}^{-2}$ . The carrier chip was then transferred back into the TEM in the same orientation to image the nanowire after doping. The concurrent implantation/imaging steps were repeated multiple times to build up the step-wise increase in the dose. The maximum implantation dose in our studies was  $1.14 \times 10^{14}$  ions  $\text{cm}^{-2}$  which corresponds to 6 successive steps. Ion beam

simulations in Ge nanowires were done by using iradina code. Further details on simulation procedures are given in the SI.

A Gatan 628 single tilt heating holder was used for all in-situ heating experiments. The same areas of the nanowires that were implanted with Ga-ions were localised and imaged at high temperature within the TEM. Sequences of images were recorded at a set temperature.

## Results and discussion

Fig. 1 shows cross-sections of three different nanowires, all approximately 45 nm in diameter, subjected to an increasing Ga-ion dose at 30 kV. The extent of crystal damage in the nanowires at fixed implantation energy can be directly related to the ion-beam fluency used. In particular, at a fluency of  $1.9 \times 10^{13}$  ions  $\text{cm}^{-2}$  (Fig. 1a and d), the arc of crystal damage shows large contrast variations due to lattice distortions resulting from clustering of point defects. At the same fluency of  $1.9 \times 10^{13}$  ions  $\text{cm}^{-2}$ , small amorphous pockets (shown with an arrow in Fig. 1d) were also observed. Such amorphous regions (3 - 5 nm in size) were also seen at the nanowire surface imaged at lattice resolution with the electron beam perpendicular to the longitudinal direction of the nanowires (SI Fig. S2 and S3). With the increase of the implantation fluency by 2 and 3 times (Fig. 1b and c), a further increase of the top surface damage depth from approximately 18 nm to 25 and 34 nm, respectively, in the form of full amorphisation towards the interior of the nanowires was observed.

Additionally, Fig. 1 demonstrates gradual decrease in the roughness of the amorphous to crystalline interface as a function of increasing fluency. Intrinsic (111) stacking fault defects present in some of the Ge nanowires (SI Fig. S4a), produced during their growth did not alter the extent and type of the ion beam damage caused upon

irradiation. Importantly, the analysis of the crystal damage was done post-factum, with no account of the initial nanowire structure and orientation towards the incoming ion beam. Conventionally, when implanting planar substrates the orientation of the incoming ion beam to the crystal is known, set at an angle (about 7 degrees off normal direction) to minimize unwanted channeling effects.

A procedure to accurately follow the evolution of crystal damage in nanowires was developed based on a correlative analysis approach,<sup>33</sup> using a carrier chip platform with markers that facilitated exchange between the TEM and FIB/SEM instruments (SI, Fig. S1). Fig. 2 represents the evolution of damage build-up in a 38 nm Ge nanowire with a step-wise increase in the Ga-ion dose at 30 kV, starting at a minimum fluency (step) of  $1.9 \times 10^{13}$  ions  $\text{cm}^{-2}$ . The nanowire was first imaged in the TEM to obtain information about crystallinity and its orientation towards the incoming electron beam. Although most of the examined nanowires were defect free and grown along the [111] direction, in order to demonstrate the capabilities of our visualisation methodology a [211] grown Ge nanowire with a set of stacking fault defects along the [111] direction was selected. A cross-section of an equivalent nanowire, having the same type of intrinsic defects and growth orientation but with a larger diameter, is presented in SI Fig. S4a. The carrier chip was first tilted to approximately 8 degrees (in one direction) to image the nanowire close to its [110] zone direction. After transferring to the SEM/FIB instrument the sample was imaged first with the SEM to localize and orient the carrier chip with the nanowire in the same direction as imaged in the TEM. After tilting the stage to 52 degrees (ion beam in a normal direction to the carrier chip) successive ion irradiation was performed at a known tilt angle, *i.e.* 8 degrees away from the (110) zone axis.

Following ion implantation, the nanowire sample was transferred back to the TEM and imaged along the same zone axis to visualise

sustained structural transformations. These sequences were repeated several times to build-up the implantation dose and obtain images monitoring the consecutive transformations. At the lowest Ga-ion fluency used (Fig. 2b) lattice distortions as well as amorphous regions (about 5 nm in size) were observed in comparison to the initial single crystalline nanowire. By further multiplying the initial ion fluency of  $1.9 \times 10^{13}$  ions  $\text{cm}^{-2}$  by 2, 3 and 4 times, the amount of amorphous regions increased, breaking the stacking fault planes at the centre of the nanowire and transforming almost the whole volume of the nanowire amorphous. These transformations were unevenly distributed along the nanowire length. At the highest fluency used, the resultant amorphous nanowire contained isolated crystalline domains in the sub-10 nm range, with the same orientation as the initial single crystal structure, as seen from the lattice resolution images (Fig. 2f); some slightly misoriented domains were also observed. Taking into account the cross-sectional data, one can envision that these crystalline islands would be predominantly located towards the middle and bottom (bottom is defined as the side opposite to the incoming ion beam) of the nanowire. These data collaborate very well to the simulations by iradina (SI Fig. S5a-d), where the lowest number of atom displacements for a 45 nm nanowire was seen in the middle and bottom of the nanowire cross-section. In comparison, a larger diameter Ge nanowire (64 nm, grown along [111] direction with prominent stacking fault defects along [11-1] direction) implanted with successive Ga-ion doses of  $1.9 \times 10^{13}$  to  $7.6 \times 10^{13}$  ions  $\text{cm}^{-2}$ , close to the same (110) zone axis, displayed an increase in lattice distortions and build-up of amorphous pockets, increasing in size from 3 to 10 nm at the side surfaces (Fig. 3). For this large diameter nanowire, extended amorphisation was not observed even at a dose as high as  $1.1 \times 10^{14}$  ions  $\text{cm}^{-2}$ .

Using our visualisation methodology, the evolution of crystal damage was monitored for 10 different nanowires with diameters ranging between 25 and 65 nm for a step-wise increase of the Ga-ion dose at 30 kV from  $1.9 \times 10^{13}$  to  $1.1 \times 10^{14}$  ions  $\text{cm}^{-2}$ . For the largest (>50 nm) diameter nanowires, crystal damage scaled with Ga-ion fluency but full amorphisation was not observed even at the highest fluency used. However, the uniform distribution of lattice point defects in the remaining crystalline part of the nanowires increased gradually with an increase of the ion dose, as seen by the weak beam dark field imaging (SI, Fig. S3a and b). For the nanowires in the 30-50 nm range the evolution of the crystal damage was equivalent to the sequence of images depicted in Fig. 2. Whereas the 25-30 nm wires were almost fully amorphised (with remaining < 5nm crystallites) even at the lowest fluency ( $1.9 \times 10^{13}$  ions  $\text{cm}^{-2}$ ) used (SI Fig. S6a and b, and Fig S7a and b).

To examine the possibility of lower energy implantations and corresponding evolution of the crystal damage in small diameter nanowires (< 25 nm), ion implantations at 5 kV were performed. Due to the drastically limited range of interactions of Ga-ions with Ge at 5 kV, the largest number of atom displacements were predicted at about 5 – 8 nm from the surface (SI Fig. S5 e-h). Hence step-wise increase in the ion fluency can be used to build-up crystal damage in analogy to 30 kV implantations in Ge nanowires with diameters >30 nm. Fig. 4 presents a sequence of images for a 22 nm Ge nanowire (including a thin 1.3 nm native oxide) subjected to an increasing Ga-ion fluency at 5 kV. Although the damage build-up followed a similar trend as for the 30 kV implantations, *e.g.* amorphisation starting at the nanowire surface after forming defects, there are several morphological differences. The increasing ion fluency resulted in a reduced nanowire diameter from 22 nm to  $16 \pm 3$  nm, forming undulating facets, while the remaining crystalline nanowire interior appeared less distorted with reduced number of domains

containing crystal defects, in comparison to the 30 kV implantations. The amorphisation was predominantly localised at the nanowire surface and progressed with gradual decrease of the crystalline core of the nanowire from 20 to  $8 \text{ nm} \pm 3 \text{ nm}$  for dose increase of 1.9 to  $5.7 \times 10^{13} \text{ ions cm}^{-2}$ . A further increase in the ion fluency resulted in further consumption of the nanowire due to amorphisation and subsequent knock-out damage from the nanowire surface (SI, Fig. S7d).

Similar to flat substrates (SI Fig. S8) the amount of crystal damage in the Ge nanowires scaled with the Ga-ion energy and fluency, however, in our study we recorded several phenomenological differences that are solely related to nanowires. Firstly, the amount and profile of the incurred ion beam damage, at a set energy and fluency, is strongly dependent on nanowire size. The thickness of the damage arcs is not conformal; much wider at the top of the nanowire cross-section where the ion beam is normal to the nanowire surface and narrower where the beam is at an oblique or parallel direction. In contrast, flat substrates normally exhibit uniform crystal damage across the whole surface. This non-conformal damage profile, which is in full agreement with the atom displacement maps obtained by irradiation, can be understood by looking at the cascade recoils in the nanowires (SI Fig. S5). Cascade recoils initiated by the ion beam that are normal to the nanowire surface terminate in the bulk of the nanowire after losing their energy. In comparison, the recoils that are localised near the side surfaces (absent in flat substrates) can exit the volume of the nanowire thus diminishing the probability of atom displacements. Specifically at lower energies, e.g. 5 kV, the range of cascade recoils is concentrated in approximately 5 - 8 nm of the nanowire surface. Hence, a large implantation dose will not only induce extended amorphisation in these regions but will also promote greater knock-out damage, as seen in our experiments. The unusual distribution of the cascade

recoils in nanowires, in comparison to planar substrates, can be used to explain the observed uneven distribution of amorphisation pockets along the length of the nanowires. Irradiation does not predict any variations in the ion interactions in the axial direction of the nanowires as the periodic boundary conditions along this direction are kept constant.

On the other hand there are aspects of the crystalline to amorphous transition in nanowires that are similar to planar Ge substrates. The formation of the amorphous phase in Si and Ge substrates due to ion bombardment has been associated with the formation of a large number of point defects, including local rearrangement of bonds (IV pair defects), which when reaching a critical density spontaneously relax towards the amorphous phase.<sup>34</sup> At a low Ga-ion fluency, as shown in our studies, lattice distortions in the form of large numbers of clustered point defects were found (SI Fig. S2),<sup>35</sup> and amorphous pockets which at higher fluencies merged into extended amorphous regions. The spatial distribution of these regions is dictated by the geometry of the nanowires leading to unusual, in comparison to planar substrates, distribution of the collision cascades. The transformation process described herein is different to the crystalline to amorphous transitions observed previously by in-situ TEM for single crystalline nanowires under incremental increase of mechanical (bending) stress. During these mechanical influences the formation and movement of dislocations towards the region that is transformed into the amorphous phase has been observed.<sup>36</sup>

In order to examine Ge nanowire crystal recovery, the same nanowire from Fig. 2 was thermally annealed in-situ in the TEM at 490 C. The remaining crystalline islands, identified as the dark regions in Fig. 5 are approx. 10 nm in diameter and located, at the back and middle of the nanowire with respect to the direction of the incoming beam as discussed before. These crystallites are the only remaining "seed" available for the crystal regrowth.<sup>28</sup>

As seen from the sequence of images in Fig. 5, the crystallites grow in size after developing recrystallisation fronts in the surrounding amorphous region. Self-nucleation of crystallites in the amorphous regions can also not be excluded. The final image in Fig. 5 shows the nanowire after 45 min at 490 C with corresponding lattice resolution images in Fig. 6. The crystallisation process resulted in a complex mixture of a large number of extended defects; mainly (111) stacking faults including the recovery of the stacking fault sequence that existed before the irradiation (see Fig. 2a for comparison). Although, the majority of the newly formed (111) stacking faults were pinned to the nanowire surface (shown with black arrows), some are parallel to the side wall facets and the initial stacking fault sequence (shown with white arrows). At the regions where these defects overlap a complex pattern is formed (marked with dashed boxes), that can be understood as interference patterns due to overlapping twinned grains.<sup>37</sup> Interestingly, the majority of the newly formed (111) stacking faults formed an ordered arrangement, similar to stacking faults identified in grown nanowires previously.<sup>31</sup>

<sup>38</sup> The crystallisation nucleated from separate crystal islands. The growth results in epitaxial recovery until recrystallisation fronts meet, forming a planar defect. Obtained recrystallisation data collaborate very well with the molecular dynamics simulations obtained for Si nanowires.<sup>32</sup> The appearance of newly formed defects and recovery of the parent crystal can be attributed to two separate processes: (i) epitaxial propagation of recrystallisation fronts (fastest growing in the (110) and (100) directions, as predicted previously<sup>39</sup>) and (ii) the interaction of these fronts when self-intersected and with the nanowire surface. These two processes result in formation of (111) stacking fault defects as well as epitaxial recovery of the rest of the nanowire including pre-existing defects. The fact that the majority of the newly formed stacking faults are pinned to the nanowire surface suggests that the surface plays a predominant role in defect formation.

## Conclusions

In this study we present visualisation methodology for mechanistic understanding of ion beam induced damage and subsequent crystal recovery in nanowires. Significantly, using developed correlative analysis platform, detailed recrystallisation data (Figure 5) were recorded in the same region of the nanowire that has been ion-beam damaged (Figure 2); hence allowing us to directly correlate structural transformations as result of ion beam damage and thermal annealing. Analysing sustained structural transformations upon ion irradiation we establish that there are morphological differences in the Ga-ion beam damage of Ge nanowires suggesting that critical defect densities, corresponding critical damage energy, knock-out damage and dynamic annealing effects are altered to those known for planar substrates. We postulate that the obtained ion implantation data using Ga-ion beams as a probe to induce structural transformations can be used to comprehend the final degree of damage in Ge nanowires but also in other nanostructured Ge materials induced by any heavy ions. Critical damage energy (5eV/at) in Ge substrates is found to be independent of the density of the cascades induced by different ions and energies.<sup>29, 40</sup> A critical damage energy density (CDED) model for ion implantation in nanostructures is important to establish and compare with bulk but this is beyond the scope of this study. A variation in energy, dopant atom, temperature and also dimensions of a nanostructure would be required for a sufficient study.

Following recrystallisation dynamics in ion-damaged Ge nanowires we presented first experimental data on the discrete steps in nanowire crystal recovery. Obtained data corresponds very well to that predicted by molecular dynamics simulations reported previously for nanowires and details the formation of stacking fault defects and their complex distribution in the nanowire volume. Moreover it is important in terms of programmable defect

engineering, e.g. formation of different Ge poly-types such as, for example, hexagonal Ge, to establish the conditions for the formation of these stacking faults. On the other hand, it is clear from this study that achieving defect free annealing of ion-doped nanostructures is more challenging and complex than for planar substrates and deserves further detailed study.

## Acknowledgements

We acknowledge financial support from the Science Foundation Ireland (Grants: 09/SIRG/I1623 and 09/IN.1/I2602).

## Notes and References

<sup>a</sup> Materials Chemistry and Analysis Group, Tyndall National Institute and the Department of Chemistry, University College Cork, Ireland.

<sup>b</sup> Centre for Research on Adaptive Nanostructures and Nanodevices (CRANN), Trinity College Dublin, Dublin 2, Ireland.

† \*Corresponding author: Address: Tyndall National Institute, Lee Maltings, Cork, Ireland. Tel: +353 214205713. Email: nikolay.petkov@tyndall.ie. Electronic supplementary information (ESI) available: See DOI: 10.1039/b000000x/

1. Y. Huang, X. F. Duan, Y. Cui, L. J. Lauhon, K. H. Kim and C. M. Lieber, *Science*, 2001, **294**, 1313-1317.
2. Y. Cui, X. F. Duan, J. T. Hu and C. M. Lieber, *Journal of Physical Chemistry B*, 2000, **104**, 5213-5216.
3. J. Michel, J. Liu and L. C. Kimerling, *Nature Photonics*, 2010, **4**, 527-534.
4. Y. Cui, Q. Q. Wei, H. K. Park and C. M. Lieber, *Science*, 2001, **293**, 1289-1292.
5. B. Tian, X. Zheng, T. J. Kempa, Y. Fang, N. Yu, G. Yu, J. Huang and C. M. Lieber, *Nature*, 2007, **449**, 885-U888.
6. R. Yan, D. Gargas and P. Yang, *Nature Photonics*, 2009, **3**, 569-576.
7. I. Ferain, C. A. Colinge and J.-P. Colinge, *Nature*, 2011, **479**, 310-316.
8. J. P. Colinge, A. Kranti, R. Yan, C. W. Lee, I. Ferain, R. Yu, N. D. Akhavan and P. Razavi, *Solid-State Electronics*, 2011, **65-66**, 33-37.
9. N. Fukata, R. Takiguchi, S. Ishida, S. Yokono, S. Hishita and K. Murakami, *Acs Nano*, 2012, **6**, 3278-3283.
10. P. Das Kanungo, R. Koegler, K. Nguyen-Duc, N. Zakharov, P. Werner and U. Goesele, *Nanotechnology*, 2009, **20**.
11. A. Colli, A. Fasoli, C. Ronning, S. Pisana, S. Piscanec and A. C. Ferrari, *Nano Letters*, 2008, **8**, 2188-2193.
12. P. Das Kanungo, R. Koegler, N. Zakharov, P. Werner, R. Scholz and W. Skorupa, *Crystal Growth & Design*, 2011, **11**, 2690-2694.
13. J. R. Haynes and W. Shockley, *Physical Review*, 1951, **81**, 835-843.
14. R. Duffy, M. Shayesteh, B. McCarthy, A. Blake, M. White, J. Scully, R. Yu, A. M. Kelleher, M. Schmidt, N. Petkov, L. Pelaz and L. A. Marques, *Applied Physics Letters*, 2011, **99**.
15. S. Biswas, C. O'Regan, N. Petkov, M. A. Morris and J. D. Holmes, *Nano Letters*, 2013, **13**, 4044-4052.
16. R. Yu, Y. M. Georgiev, S. Das, R. G. Hobbs, I. M. Povey, N. Petkov, M. Shayesteh, D. O'Connell, J. D. Holmes and R. Duffy, *physica status solidi (RRL) – Rapid Research Letters*, 2014, **8**, 65-68.
17. C. Borschel and C. Ronning, *Nuclear Instruments & Methods in Physics Research Section B-Beam Interactions with Materials and Atoms*, 2011, **269**, 2133-2138.
18. J. Ziegler, PARTICLE INTERACTIONS WITH MATTER, <http://www.srim.org/>.
19. C. R. C Borschel, Ion beam irradiation of 3D nanostructures-a new Monte Carlo simulation code, [www.iradina.de](http://www.iradina.de).
20. G. L. Olson and J. A. Roth, *Materials Science Reports*, 1988, **3**, 1-77.
21. R. Drosd and J. Washburn, *Journal of Applied Physics*, 1982, **53**, 397-403.
22. R. Duffy, M. J. H. Van Dal, B. J. Pawlak, M. Kaiser, R. G. R. Weemaes, B. Degroote, E. Kunnen and E. Altamirano, *Applied Physics Letters*, 2007, **90**, -.
23. U. Köster, *physica status solidi (a)*, 1978, **48**, 313-321.
24. Z. G. Wang, T. Kato, T. Hirayama, N. Kato, K. Sasaki and H. Saka, *Applied Surface Science*, 2005, **241**, 80-86.
25. H. Watanabe, K. Kutsuki, I. Hideshima, G. Okamoto, T. Hosoi and T. Shimura, in *Technology Evolution for Silicon Nano-Electronics*, eds. S. Miyazaki and H. Tabata, 2011, vol. 470, pp. 152-157.
26. M. Wittmer, M. A. Nicolet and J. W. Mayer, *Thin Solid Films*, 1977, **42**, 51-59.
27. H. Watanabe, K. Kutsuki, A. Kasuya, I. Hideshima, G. Okamoto, S. Saito, T. Ono, T. Hosoi and T. Shimura, *Current Applied Physics*, 2012, **12**, S10-S19.
28. Y. Wang, Y. Z. Hu and E. A. Irene, *Journal of Vacuum Science & Technology a-Vacuum Surfaces and Films*, 1994, **12**, 1309-1314.
29. A. Claverie, S. Koffel, N. Cherkashin, G. Benassayag and P. Scheiblin, *Thin Solid Films*, 2010, **518**, 2307-2313.
30. J. Tang, C.-Y. Wang, F. Xiu, A. J. Hong, S. Chen, M. Wang, C. Zeng, H.-J. Yang, H.-Y. Tuan, C.-J. Tsai, L. J. Chen and K. L. Wang, *Nanotechnology*, 2010, **21**, 505704.
31. S. Barth, J. J. Boland and J. D. Holmes, *Nano Letters*, 2011, **11**, 1550-1555.
32. L. A. Marques, L. Pelaz, I. Santos, P. Lopez and R. Duffy, *Journal of Applied Physics*, 2012, **111**.
33. J. M. Stiegler, R. Tena-Zaera, O. Idigoras, A. Chuvilin and R. Hillenbrand, *Nature Communications*, 2012, **3**.
34. A. Claverie, C. Vieu, J. Faure and J. Beauvillain, *Journal of Applied Physics*, 1988, **64**, 4415-4423.
35. R. Rettig, S. Steuer and R. F. Singer, *Journal of Phase Equilibria and Diffusion*, 2011, **32**, 198-205.
36. S. Decoster and A. Vantomme, *Journal of Physics D: Applied Physics*, 2009, **42**, 165404.
37. H. Bender, A. Deveirman, J. Vanlanduyt and S. Amelinckx, *Applied Physics a-Materials Science & Processing*, 1986, **39**, 83-90.
38. Z. Su, C. Dickinson, Y. Wan, Z. Wang, Y. Wang, J. Sha and W. Zhou, *CrystEngComm*, 2010, **12**, 2793-2798.
39. M. Posselt and A. Gabriel, *Physical Review B*, 2009, **80**.
40. M. S. Yeh, Y. J. Lee, M. F. Hung, K. C. Liu and Y. C. Wu, *Ieee Transactions on Nanotechnology*, 2013, **12**, 636-640.

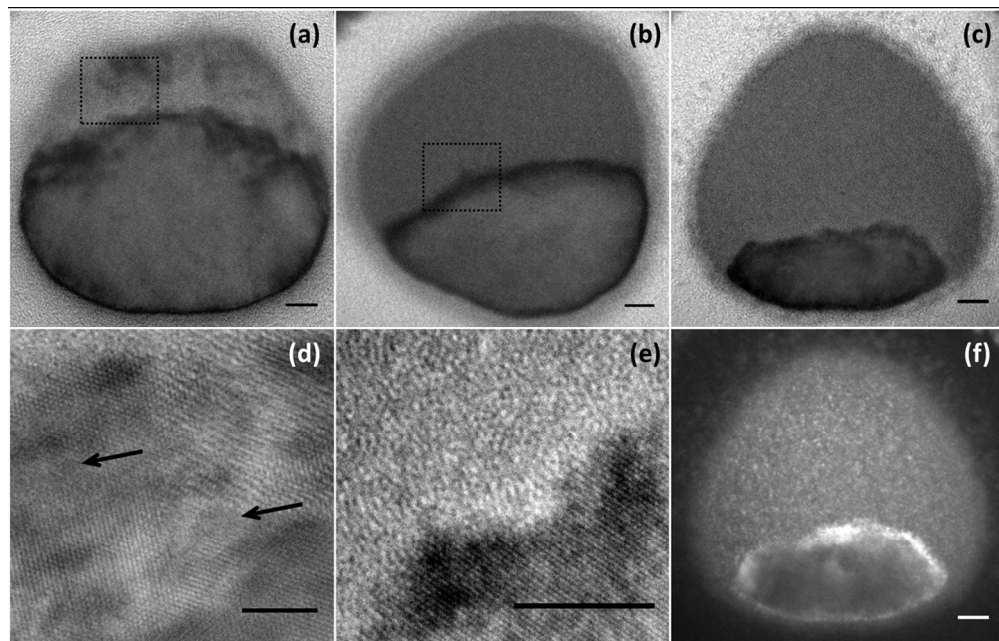


**Fig. 1.** Cross-sectional TEM images of different Ge nanowires of approximately 45 nm in diameter after irradiation at 30 kV with increasing Ga-ion fluencies of (a)  $1.9 \times 10^{13}$ , (b)  $3.8 \times 10^{13}$  and (c)  $5.7 \times 10^{13}$  ion  $\text{cm}^{-2}$ . All scale bars are 5 nm. (d) and (e) Lattice resolution TEM images taken from the marked areas in (a) and (b), respectively. (f) Weak beam dark field TEM image of the same nanowire as in (c) taken under  $g$ ,  $2g$  with  $g = 220$  conditions. In all images, the direction of the ion flux is from the top and the cross-sections were imaged close to the  $[111]$  zone direction. Arrows in (d) mark small amorphous pockets. Scale bar for all images is 5nm.

254x162mm (150 x 150 DPI)

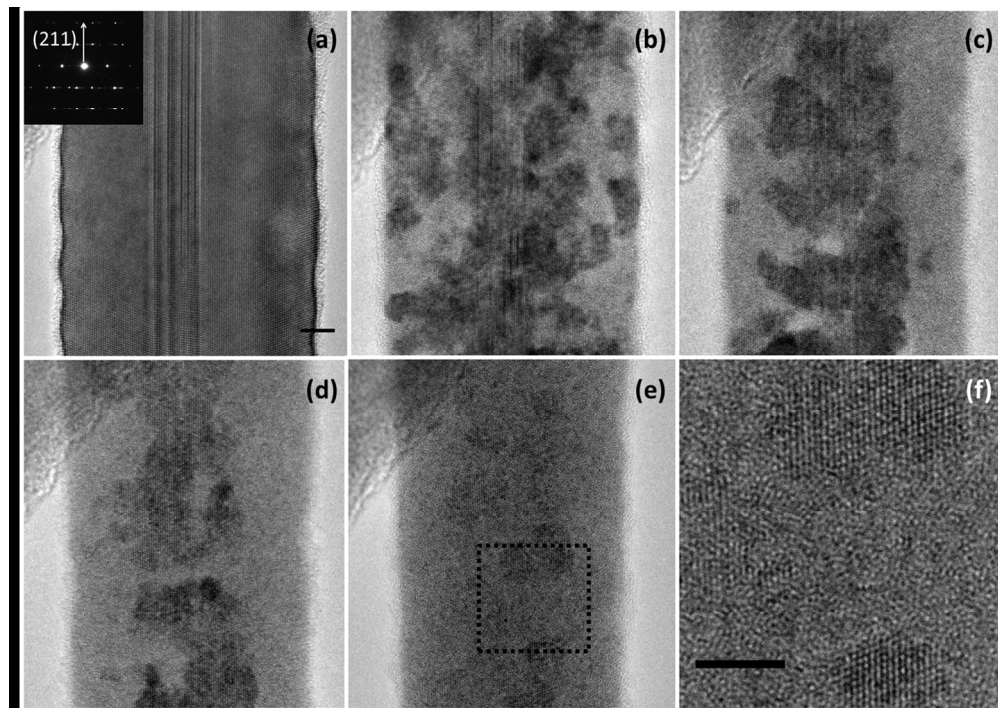


**Fig. 2.** Step-wise irradiation of a 38 nm diameter Ge nanowire with a 30 kV Ga-ion beam. (a) Initial nanowire before irradiation imaged close to the [110] zone axis, inset demonstrating complex SAED due to longitudinal (111) stacking fault defect. (b - e) Images of the same area taken close to the same zone direction after irradiation with increasing fluency of (b)  $1.9 \times 10^{13}$ , (c)  $3.8 \times 10^{13}$ , (d)  $5.7 \times 10^{13}$  and (e)  $7.6 \times 10^{13}$  ion  $\text{cm}^{-2}$ . All images were taken at the same magnification. (f) Lattice resolution TEM image of the area marked in (e), demonstrating crystal domains orientated in the same [110] direction as the initial nanowire. Scale bar for all images is 5nm.

254x178mm (150 x 150 DPI)

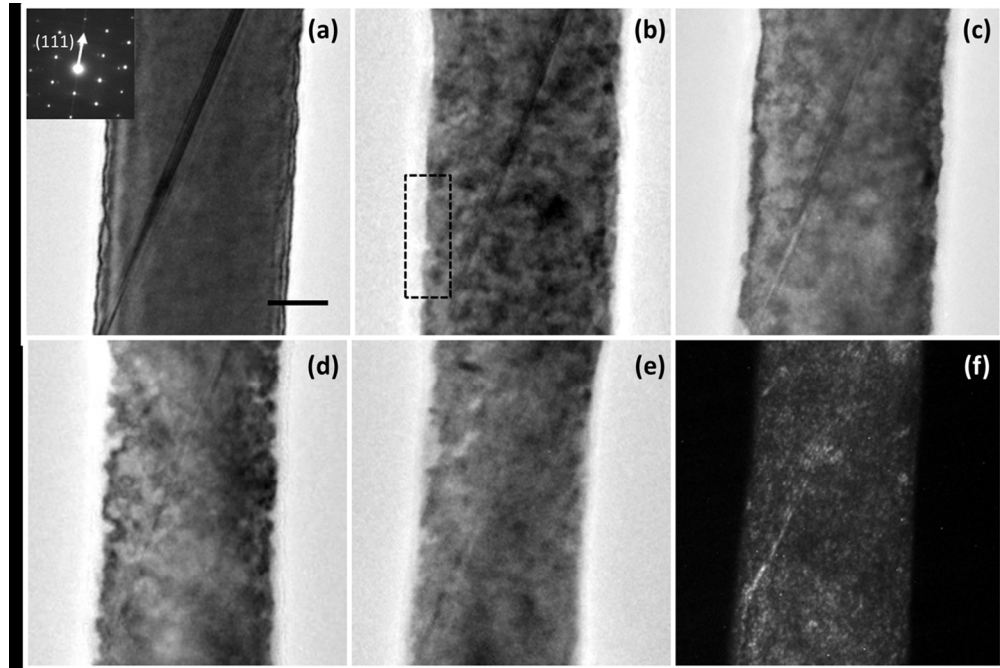


**Fig. 3.** Consecutive 30 kV Ga ion irradiations of a 64 nm diameter Ge nanowire with a beam tilted about 3 degrees off the [110] zone direction. (a) Initial nanowire before irradiation imaged close to the [110] zone axis, inset SAED pattern taken away from the defect. (b - e) Images of the same area taken close to the same zone direction after irradiation, with an increasing fluency of  $1.9 \times 10^{13}$ ,  $3.8 \times 10^{13}$ ,  $5.7 \times 10^{13}$  and  $7.6 \times 10^{13}$  ion  $\text{cm}^{-2}$ . All images are taken at the same magnification. (f) weak beam dark field image taken under  $g$ ,  $2g$  with  $g = 220$  conditions demonstrating most of the stacking fault defects are still present after irradiation. Scale bar for all images is 20nm.  
254x169mm (150 x 150 DPI)

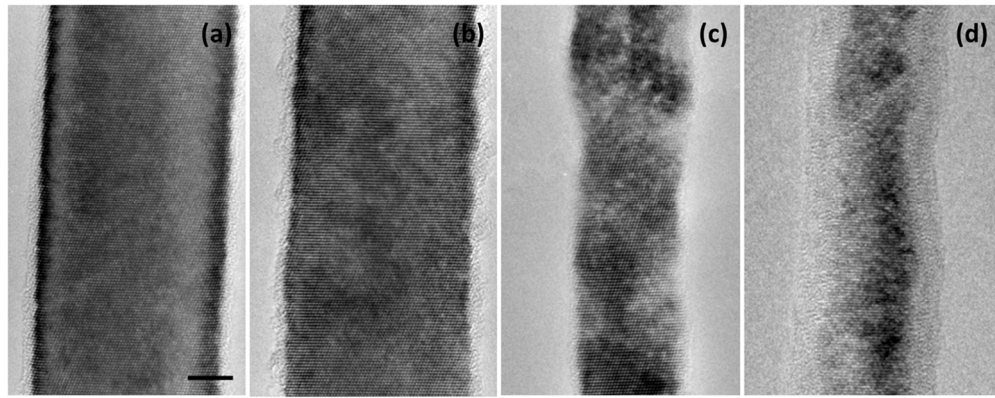


**Fig. 4.** Step-wise irradiation of a 22 nm diameter Ge nanowire with a 5 kV Ga-ion beam. (a) Initial nanowire before irradiation imaged close to the [110] zone axis. (b - e) Images of the same area taken close to the same zone direction after irradiation with increasing fluency of  $1.9 \times 10^{13}$ ,  $3.8 \times 10^{13}$ ,  $5.7 \times 10^{13}$  and  $7.6 \times 10^{13}$  ion  $\text{cm}^{-2}$ . All images were taken at the same magnification. Scale bar for all images is 5nm. The direction of the incoming Ga-ion beam during implantation was 5 degrees off the [110] direction.  
254x101mm (150 x 150 DPI)

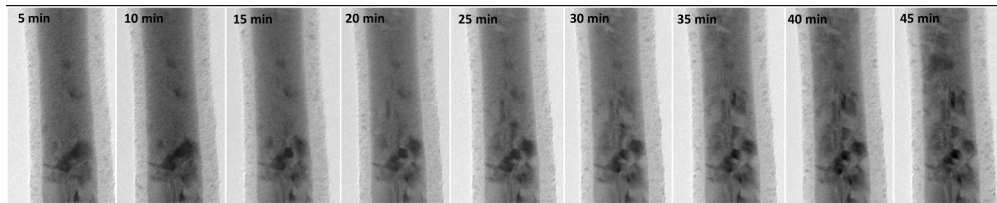


**Fig. 5.** In-situ anneal of nanowire after final implantation dose of  $7.6 \times 10^{13}$  ions  $\text{cm}^{-2}$  at 490 C. 495x98mm (150 x 150 DPI)

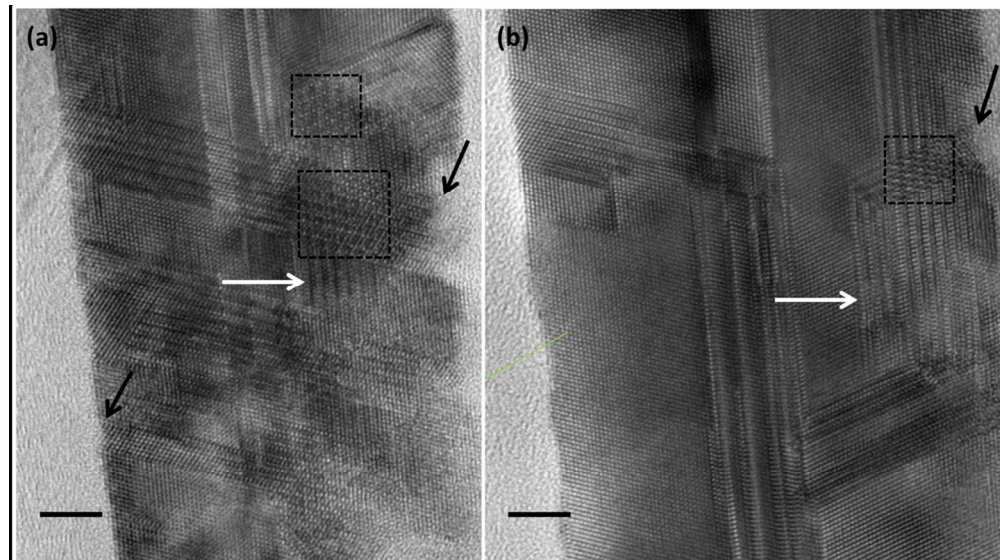


**Fig. 6.** Lattice resolution images of nanowire post recrystallisation at (a) region of interest showing a high density of stacking fault defects as well as an increase in edge roughness. In another region of the same nanowire (b) a mixture of in-borne defect curing, high density defect formation and retention of original crystal structure are all observed. Scale bar for all images is 5nm.  
254x142mm (150 x 150 DPI)